



































MIGHTEE: are giant radio galaxies more common than we thought?

J. Delhaize ¹★ I. Heywood ^{2,3,4} M. Prescott ⁵ M. J. Jarvis ^{2,6} I. Delvecchio ^{7,8} I. H. Whittam ^{2,6}
 S. V. White ³ M. J. Hardcastle ⁹ C. L. Hale ¹⁰ J. Afonso ^{11,12} Y. Ao ^{13,14} M. Brienza ^{15,16}
 M. Brüggén ¹⁷ J. D. Collier ^{18,19} E. Daddi ⁷ M. Glowacki ^{5,6} N. Maddox ²⁰ L. K. Morabito ²¹
 I. Prandoni ¹⁶ Z. Randriamanakoto ²² S. Sekhar ^{5,18,23} Fangxia An ⁵ N. J. Adams ² S. Blyth ¹
 R. A. A. Bowler ² L. Leuw ⁶ L. Marchetti ^{1,16} S. M. Randriamampandry ^{22,24} K. Thorat ^{18,25}
 N. Seymour ²⁶ O. Smirnov ^{3,4} A. R. Taylor ^{5,18} C. Tasse ^{27,28,29} and M. Vaccari ^{5,16}

Affiliations are listed at the end of the paper

Accepted 2020 December 9. Received 2020 November 18; in original form 2020 September 18

ABSTRACT

We report the discovery of two new giant radio galaxies (GRGs) using the MeerKAT International GHz Tiered Extragalactic Exploration (MIGHTEE) survey. Both GRGs were found within a ~ 1 deg² region inside the COSMOS field. They have redshifts of $z = 0.1656$ and $z = 0.3363$ and physical sizes of 2.4 and 2.0 Mpc, respectively. Only the cores of these GRGs were clearly visible in previous high-resolution Very Large Array observations, since the diffuse emission of the lobes was resolved out. However, the excellent sensitivity and uv coverage of the new MeerKAT telescope allowed this diffuse emission to be detected. The GRGs occupy an unpopulated region of radio power – size parameter space. Based on a recent estimate of the GRG number density, the probability of finding two or more GRGs with such large sizes at $z < 0.4$ in a ~ 1 deg² field is only 2.7×10^{-6} , assuming Poisson statistics. This supports the hypothesis that the prevalence of GRGs has been significantly underestimated in the past due to limited sensitivity to low surface brightness emission. The two GRGs presented here may be the first of a new population to be revealed through surveys like MIGHTEE that provide exquisite sensitivity to diffuse, extended emission.

Key words: galaxies: active – radio continuum; galaxies.

1 INTRODUCTION

Some classes of active galactic nuclei (AGNs) have jets of relativistic plasma/particles emanating from the central region, which produce radio synchrotron emission. In some cases, these jets propagate to extremely large distances beyond the host galaxy and into the intergalactic medium (IGM). When the projected linear size of the jets and lobes exceeds 0.7 Mpc, such systems are referred to as giant radio galaxies (GRGs; e.g. Lara et al. 2001; Schoenmakers et al. 2001; Dabhade et al. 2020a).¹ GRGs are the largest individual objects in the Universe. The largest known has a projected linear size² of 4.89 Mpc (Machalski et al. 2008), though the majority of known GRGs are below 2 Mpc in extent (Dabhade et al. 2020b).

Several factors have been proposed to explain why the jets of GRGs are able to extend to such large distances. One suggestion is that these systems exist in low-density environments that allow the jets to permeate easily through the IGM (e.g. Mack et al. 1998; Malarecki et al. 2015). However, ~ 10 per cent of GRGs have now been found to reside in cluster environments (Komberg & Pashchenko 2009;

Tang et al. 2020; Dabhade et al. 2020b) and Lan & Prochaska (2020) recently found no difference between the environments of GRGs and that of galaxy control samples. Another scenario is that the central engines of GRGs may boast particularly powerful and/or restarted AGN activity, though several studies including Komberg & Pashchenko (2009) and Hardcastle et al. (2019) found little evidence that GRGs are different to normal radio galaxies in this respect.

A prevailing idea is that these objects represent the oldest AGN systems, such that the jets have had enough time to grow to their large sizes (e.g. Ishwara-Chandra & Saikia 1999). However, we may then expect the existence of many more GRGs than are currently known (Komberg & Pashchenko 2009).

Fewer than 1000 GRGs have been found to date. Dabhade et al. (2020b) recently compiled a comprehensive catalogue of all 820 GRGs known. At the time of writing, a further six have been reported by Ishwara-Chandra et al. (2020) and five by Tang et al. (2020).

The first GRG discovery was made in the 1970s (Willis, Strom & Wilson 1974) and since then GRGs have primarily been found via wide-field radio continuum surveys such as the NRAO VLA Sky Survey (NVSS; Condon et al. 1998), the Faint Images of the Radio Sky at Twenty-Centimeters survey (FIRST; Becker, White & Helfand 1995), the Westerbork Northern Sky Survey (WENSS; Rengelink et al. 1997), and the Sydney University Molonglo Sky Survey (SUMSS; Mauch et al. 2003).

The highly extended nature of GRGs and the generally low surface brightness of their lobes, which fade as they age, make

* E-mail: jacinta@ast.uct.ac.za

¹ Adjusted to the modern cosmology of Planck Collaboration et al. (2016) for consistency with the current literature.

² Based on a redshift of $z = 0.3067$, an angular size of 17.4 arcmin, and adjusted to our chosen cosmology.

Table 1. Summary of the MeerKAT MIGHTEE observations used for this study. The COSMOS field centre is J2000 $10^{\text{h}}00^{\text{m}}28^{\text{s}}.6 + 02^{\text{d}}12^{\text{m}}21^{\text{s}}$, and the COSMOS_8 pointing is at J2000 $10^{\text{h}}00^{\text{m}}29^{\text{s}}.0 + 02^{\text{d}}33^{\text{m}}33^{\text{s}}.79$. The primary calibrator for all observations was PKS B1934–638, and the secondary was 3C 237. The observations used MeerKAT’s *L*-band system, 900–1670 MHz.

Date	Block ID	Field	Antennas	Track (h)	On-source (h)	Channels
2018-04-19	1524147354	COSMOS	64	8.65	6.1	4096
2018-05-06	1525613583	COSMOS	62	8.39	5.1	4096
2020-04-02	1585844155	COSMOS_8	60	8	6.25	32768
2020-04-26	1587911796	COSMOS	59	8	6.25	32768

them notoriously difficult to detect and identify. For example, 162 GRGs have only very recently been discovered in NVSS data, despite this survey having already existed for two decades. These were found via the Search and Analysis of Giant radio galaxies with Associated Nuclei (SAGAN) project, which rigorously combined newly developed automated pattern recognition techniques (Proctor 2016) with careful manual inspection (Dabhade et al. 2017, 2020b). Despite such efforts, and the existence of many thousands of ‘normal’ sized (<0.7 Mpc) radio galaxies (RGs), GRGs remain scarce (e.g. Kaiser, Dennett-Thorpe & Alexander 1997).

However, the new generation of deep and wide-field radio surveys, with sensitivity to a range of spatial scales, may provide a much clearer understanding of the number density and physics of such sources. In particular, low-frequency surveys with new-generation instruments like the Low-Frequency Array (LOFAR; van Haarlem et al. 2013), the Murchison Widefield Array (MWA; Tingay et al. 2013), and the upgraded Giant Metre-wave Radio Telescope (uGMRT; Gupta et al. 2017) are proving excellent resources for detecting and characterizing GRGs (e.g. Hurley-Walker et al. (e.g. Hurley-Walker et al. 2015; Hardcastle et al. 2016; Clarke et al. 2017; Cantwell et al. 2020; Seymour et al. 2020). This is due, in part, to the increasing brightness towards lower radio frequencies often displayed by radio galaxies. Indeed, Dabhade et al. (2020a) recently reported the highest sky density of consistently-sampled GRGs using Data Release 1 of the LOFAR Two-metre Sky Survey (LoTSS; Shimwell et al. 2019). They found 239 GRGs over a 424 deg^2 region at 120–168 MHz.

In the GHz regime, the newly commissioned MeerKAT telescope in South Africa (Jonas & MeerKAT Team 2016) is proving to be an excellent instrument for GRG studies (e.g. Cotton et al. 2020). Although it operates at higher frequencies than LOFAR, MWA, and uGMRT (though there is some overlap in observing frequency with the latter), MeerKAT has the excellent sensitivity and *uv* coverage ideal for such work, including the simultaneous availability of long and short baselines.

The MeerKAT International GHz Tiered Extragalactic Exploration survey (MIGHTEE; Jarvis et al. 2016) is a galaxy evolution survey underway with MeerKAT. Among its data products will be high-quality radio continuum data over a relatively wide field (20 deg^2). In this paper, we report the discovery of two newly identified GRGs in 1 deg^2 MIGHTEE Early Science observations of the COSMOS field. The discovery of these objects within such a small sky area hints at the presence of a ‘hidden’ population of GRGs, hitherto undetected due to observational limitations. If GRGs prove to be more common than previously thought, this may alter our understanding of the AGN duty cycle and the impact of AGN-induced jets on the evolution of galaxies and the IGM.

Throughout this paper, we assume a Λ cold dark matter cosmology with $H_0 = 67.8 \text{ km s}^{-1} \text{ Mpc}^{-1}$, $\Omega_\Lambda = 0.692$, and $\Omega_M = 0.308$ (Planck Collaboration et al. 2016). We assume a Chabrier (2003) initial mass function, unless otherwise stated.

2 RADIO CONTINUUM SURVEYS

2.1 MIGHTEE *L*-band data

The MIGHTEE survey targets four extragalactic deep fields, namely the European Large Area *ISO* Survey – South 1 (ELAIS-S1), COSMOS, the *XMM-Newton* Large Scale Structure (XMM-LSS) field, and the Extended Chandra Deep Field South (E-CDFS), for a total sky area of approximately 20 deg^2 . The survey uses total intensity, polarized intensity, and spectral line data products to achieve a range of science goals. It has components using MeerKAT’s *L*-band (900–1670 MHz) and *S*-band (1.75–3.5 GHz) receivers, and a primary design requirement is to reach the *L*-band classical confusion limit in total intensity at about $2 \mu\text{Jy beam}^{-1}$ (for a resolution of $\sim 8 \text{ arcsec}$).

The initial release of total intensity continuum within the MIGHTEE consortium included a single pointing in the COSMOS field (J2000 $10^{\text{h}}00^{\text{m}}28^{\text{s}}.6 + 02^{\text{d}}12^{\text{m}}21^{\text{s}}$; see Table 1). The two GRGs we present in this paper were discovered in this pointing. Since one of the GRGs was towards the edge of the field, we have also imaged an extra MIGHTEE pointing (COSMOS_8; J2000 $10^{\text{h}}00^{\text{m}}29^{\text{s}}.0 + 02^{\text{d}}33^{\text{m}}33^{\text{s}}.79$) for which this object was closer to the centre of the primary beam.

Full details of the initial MIGHTEE continuum data release and the data processing method³ will be presented in Heywood et al. (in preparation), however we provide a brief overview here.

(i) The data were converted from their native format into a MeasurementSet format by the South African Radio Astronomy Observatory (SARAO) archive,⁴ and averaged from their original *L*-band frequency resolution to 1024 channels in the process. Flags generated by the telescope control and monitoring system were applied.

(ii) Basic flagging commands were applied to all fields using CASA (McMullin et al. 2007). Frequency ranges containing persistent radio frequency interference (RFI) were flagged on spacings shorter than 600 m. The autoflagging algorithms TFCROP and RFLAG were used on the calibrator fields.

(iii) The standard calibrator PKS B1934–638 was used to derive delay and bandpass solutions using the relevant CASA tasks. This was an iterative process, with rounds of autoflagging on residual visibilities in each iteration.

(iv) The gain solutions derived from the primary were applied to the secondary calibrator (3C 237), and an intrinsic spectral model was derived for the latter. Time-dependent complex gains were then derived from the observations of the secondary using this intrinsic

³The calibration and imaging scripts are available online here: <https://www.github.com/IanHeywood/oxkat> and through the Astrophysics Source Code Library record ascl:2009.003 (Heywood 2020).

⁴<https://archive.sarao.ac.za/>

model with the GAINCAL task. This process compensates for the effects of the large fractional bandwidth of MeerKAT, coupled with the fact that the data arrive in MeasurementSet format that only has a single spectral window. The flux scale may be biased if this effect is not taken into account.

(v) All the gain corrections were applied to the target data, which is then flagged using the TRICOLOUR⁵ package. Removing the edges of the bandpass where the gain sharply rolls off results in 770 MHz of usable bandwidth. A loss of about 50 per cent of the data in this region is typical following RFI removal, although the RFI occupancy is strongly baseline dependent, and most of this loss occurs on spacings shorter than 1 km.

(vi) The target data were imaged using WSCLEAN (Offringa et al. 2014). The data were imaged blindly with 100 000 iterations, and a clean mask was derived from the resulting image, excluding regions below a local threshold of 6σ where σ is the pixel standard deviation. The data were re-imaged using this mask.

(vii) The multifrequency clean components from the masked image were used to predict a visibility model for self-calibration using the CASA GAINCAL task. Phase corrections were derived for every 64 s of data, and an amplitude and phase correction was derived for every target scan, with the solutions for the former applied while solving for the latter. The self-calibrated data were re-imaged using WSCLEAN and the mask is refined if necessary.

(viii) Direction-dependent corrections were made by imaging the data with DDFACET (Tasse et al. 2018). The resulting model was partitioned into ~ 10 directions, constrained by the location of off-axis problem sources, and the need to retain suitable flux in the sky model per direction. The KILLMS package (e.g. Smirnov & Tasse 2015) was then used to solve for a complex gain correction for each direction with a time/frequency interval of 5 min/128 channels. Another run of DDFACET reimaged the data, applying the directional corrections.

(ix) Finally, the images were primary-beam corrected by dividing them by an azimuthally averaged Stokes I model, evaluated at 1284 MHz using the EIDOS (Asad et al. 2019) package.

MIGHTEE continuum data are imaged twice, with a Briggs' robust parameter of 0.0 and -1.2 . This is to deliver a higher sensitivity image as well as a higher angular resolution image, the trade-off for which is a loss of sensitivity due to the down-weighting of the many short spacings that MeerKAT's dense core provides. The COSMOS pointing for a total on-source time of 17.45 h reaches a thermal noise (measured away from the main lobe of the primary beam) of $1.9 \mu\text{Jy beam}^{-1}$ in the robust 0.0 image, with an angular resolution of $8.4 \text{ arcsec} \times 6.8 \text{ arcsec}$ (position angle -11.2 deg). The robust -1.2 image reaches $6 \mu\text{Jy beam}^{-1}$ with an angular resolution of $4.8 \text{ arcsec} \times 4.0 \text{ arcsec}$ (position angle -12.63 deg).

We imaged the 6.25 h of COSMOS_8 data with less aggressive weighting (robust = 0.3) in order to increase the sensitivity to the diffuse emission from the lobes. This image has a thermal noise of $2.5 \mu\text{Jy beam}^{-1}$ and an angular resolution of $11.6 \text{ arcsec} \times 7.4 \text{ arcsec}$ (position angle -12.6 deg). The higher resolution map made with COSMOS_8 data was imaged using a robust parameter of -1.2 and has a thermal noise of $8.5 \mu\text{Jy beam}^{-1}$ and an angular resolution of $5.0 \text{ arcsec} \times 4.0 \text{ arcsec}$ (position angle -15.44 deg).

Note that in practice the central region of the lower resolution images (both COSMOS and COSMOS_8) are limited to root mean squared (*rms*) 'noise' levels of $\sim 3 \mu\text{Jy beam}^{-1}$ by a combination of

thermal noise and classical confusion. The lower resolution images are used for the work presented here, unless otherwise stated.

2.2 VLA-COSMOS 3 GHz Large Project

In this paper, we also use data from the VLA-COSMOS 3 GHz Large Project (hereafter VLA-3 GHz). This project was presented by Smolčić et al. (2017a) and is a continuum survey with the Karl G. Jansky Very Large Array (VLA; Perley et al. 2011) covering 2.6 deg^2 over the full COSMOS field. This 384 h survey was centred at 3 GHz with a 2 GHz bandwidth using three sets of 64 pointings in A and C array. It reached an *rms* sensitivity of $2.3 \mu\text{Jy beam}^{-1}$ with 0.75 arcsec resolution. This is similar in sensitivity to the Early Science MIGHTEE data, accounting for the different central frequencies and assuming a standard spectral index for radio galaxies ($\alpha = -0.8$; where $S_\nu \propto \nu^\alpha$).

While the angular resolution of the VLA-3 GHz data is superior to that of MIGHTEE, it has poorer sensitivity to large-scale emission. The VLA has up to 351 baselines with a minimum baseline length of 36 m, while MeerKAT has up to 2016 baselines with a minimum length of 29 m. The larger number of short baselines, combined with the better instantaneous *uv* coverage provided by its configuration, therefore makes MeerKAT the better instrument for detecting diffuse, extended emission.

3 GRG PROPERTIES

The two GRGs were serendipitously discovered in the MIGHTEE-COSMOS map (original pointing) during the process of cross-matching the radio sources with their optical counterparts, via visual inspection. Details of this process will be presented in Prescott et al., (in preparation), and are similar to those of Prescott et al. (2018). Following IAU conventions, we name these sources MGTC J095959.63+024608.6 (hereafter GRG1) and MGTC J100016.84+015133.0 (hereafter GRG2). The prefix MGTC indicates the discovery of the sources in the MIGHTEE-continuum survey. The basic properties of each GRG are summarized in Table 2 and flux densities and radio powers are presented in Table 3. Note that only statistical uncertainties are quoted in Table 2, but that systematic uncertainties are found to be less than 3 per cent (Heywood et al., in preparation).

3.1 MGTC J095959.63+024608.6 (GRG1)

3.1.1 MIGHTEE data

GRG1 is shown in Figs 1–3. The two diffuse outer lobes and jets are detected for the first time in MIGHTEE, thus newly identifying this object as a GRG. The core of GRG1 is located at RA = $09^{\text{h}}59^{\text{m}}59^{\text{s}}.63$ and Dec. = $+02^{\text{d}}46^{\text{m}}08^{\text{s}}.6$ and has an elongated structure in MIGHTEE. It is associated with a host galaxy identified in optical and near-infrared data (see Fig. 2 inset) with a spectroscopic redshift of $z = 0.1656$, according to the Sloan Digital Sky Survey Data Release 14 (SDSS DR14; Abolfathi et al. 2018). Summing the distance between the outer edges of each lobe and the central core, the total projected angular size of GRG1 is 13.8 arcmin. It therefore has a physical size of 2.42 Mpc, which places it solidly in the regime of giant radio galaxies.

The northern lobe contains a potential hot-spot which is extended and is not associated with any point source (indicated in Fig. 1). This is confirmed using the higher-resolution ($4.8 \text{ arcsec} \times 4.0 \text{ arcsec}$) MIGHTEE image. A comparison with optical data (Prescott et al.,

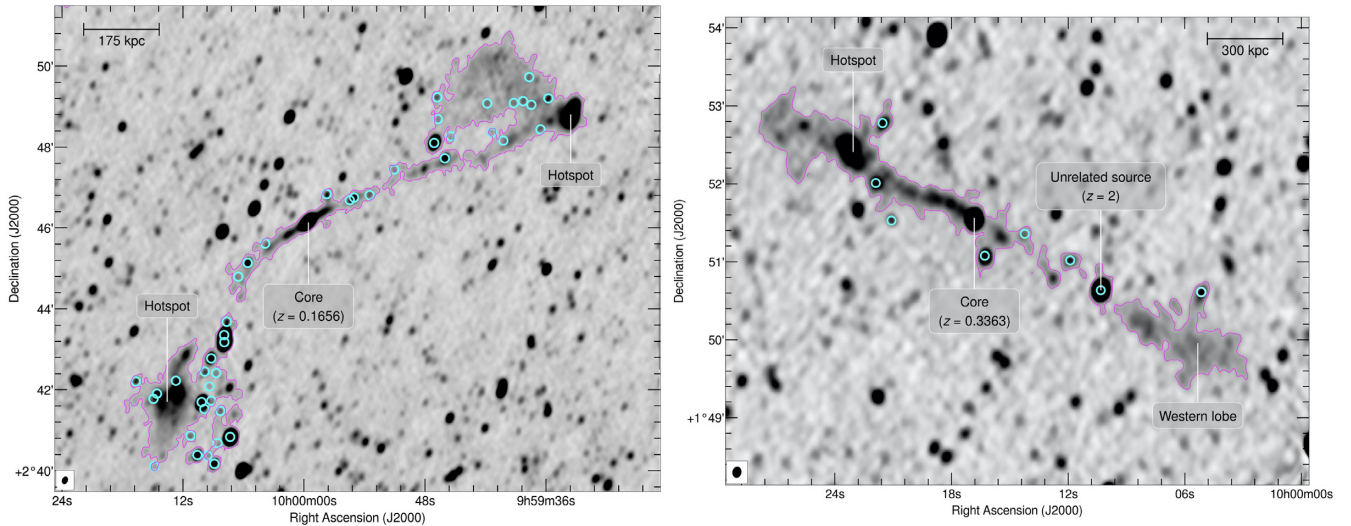
⁵<https://github.com/ska-sa/tricolour>

Table 2. Properties of the two GRGs discovered in MIGHTEE-COSMOS. Columns: (1) Object name, (2) right ascension (J2000), (3) declination (J2000), (4) spectroscopic redshift, (5) projected angular size, (6) projected linear size.

1	2	3	4	5	6
Name	RA (h:m:s)	Dec. (d:m:s)	z	d (arcmin)	D (Mpc)
MGTC J095959.63+024608.6 (<i>GRG1</i>)	09:59:59.63	+02:46:08.6	0.1656	13.8	2.42
MGTC J100016.84+015133.0 (<i>GRG2</i>)	10:00:16.84	+01:51:33.0	0.3363	6.8	2.04

Table 3. Integrated flux and radio power of the two GRGs. Columns: (1) Object name, (2) effective frequency of MIGHTEE map at position of GRG, (3) peak brightness of core, (4–6) integrated flux density of core, northern lobe, and southern lobe, (7) total integrated flux density of GRG, combining all components, (8) spectral index of core, (9) radio power at ν_{eff} (~ 1.2 GHz), based on columns 7 and 8.

1	2	3	4	5	6	7	8	9
Name ^a	ν_{eff} (GHz)	$S_{\text{p,core}}$ (mJy beam ⁻¹)	$S_{\text{int,core}}$ (mJy)	$S_{\text{int,NL}}$ (mJy)	$S_{\text{int,SL}}$ (mJy)	$S_{\text{int,all}}$ (mJy)	$\alpha_{3\text{GHz}}^{\nu_{\text{eff}}}$	$P_{1.2\text{GHz}}$ (WHz ⁻¹)
GRG1	1.217	3.73 ± 0.01	5.92 ± 0.01	8.59 ± 0.02	$21.07 \pm 0.01^{\text{b}}$	$35.59 \pm 0.02^{\text{b}}$	-0.51 ± 0.03	$(2.438 \pm 0.002) \times 10^{24\text{b}}$
GRG2	1.256	0.72 ± 0.01	0.778 ± 0.002	2.04 ± 0.01	0.92 ± 0.01	3.74 ± 0.02	0.29 ± 0.04	$(1.329 \pm 0.007) \times 10^{24}$

^aSee Table 2 for official names.^bMay include significant levels of unrelated emission from coincident continuum sources. See text for details.**Figure 1.** GRG1 (left) and GRG2 (right) as seen in MIGHTEE. The magenta contour (for GRG-associated emission only) highlights the full extent of the GRGs. The contour level is $7 \mu\text{Jy beam}^{-1}$ for GRG1 and $5 \mu\text{Jy beam}^{-1}$ for GRG2. Notable features of the GRGs are labelled. Unrelated continuum sources are marked by cyan circles. The MIGHTEE maps shown are COSMOS.8 (robust = 0.3, thermal noise $2.5 \mu\text{Jy beam}^{-1}$) for GRG1, and COSMOS (robust = 0.0, thermal noise $1.9 \mu\text{Jy beam}^{-1}$) for GRG2. The beam is shown in the bottom left corner of each image.

in preparation) likewise reveals no counterpart. Diffuse emission extends to the north-east of this hotspot, in a direction perpendicular to that of the jet. The reason for this is unclear, but could indicate interactions with the surrounding IGM, allowing plasma to flow in that direction (e.g. Subrahmanyam et al. 2008). This lobe appears to be edge-brightened, which is typical of a Fanaroff and Riley type II (FR II; Fanaroff & Riley 1974) radio galaxy. Some collimated jet emission is present between the core and the lobes.

There is also evidence of a potential hotspot towards the centre of the southern lobe and the presence of a jet. The latter is bent with respect to the northern jet alignment. Again, this could be due to interactions with the IGM and surrounding environment. For example, Malarecki et al. (2015) suggest that the lobes of GRGs could bend to avoid high-density regions.

MIGHTEE flux densities in Table 3 are measured by integrating within the region indicated by the magenta contour shown in Fig. 1.

The contributions from coincident compact continuum sources not associated with the GRG have been removed. These unrelated sources (presumably fore- or background galaxies) are marked in Fig. 1 and were identified in the counterpart cross-matching procedure of Prescott et al. (in preparation). This made use of the higher-resolution MIGHTEE and VLA-3GHz data. Except for continuum sources larger than the beam, we assume they are unresolved point sources and approximate their total flux density to be equal to their peak brightness in the higher-resolution MIGHTEE map. This is to minimize the amount of diffuse GRG-related emission removed.

However, some ‘contaminating’ emission from these unrelated sources may still remain, meaning that the flux density measurements in Table 3 are conservative upper limits, particularly for the southern lobe. A lower limit for the flux density of the southern lobe (avoiding areas with bright continuum sources) is 3.60 ± 0.01 mJy, giving a total flux density for GRG1 of 18.11 ± 0.02 mJy.

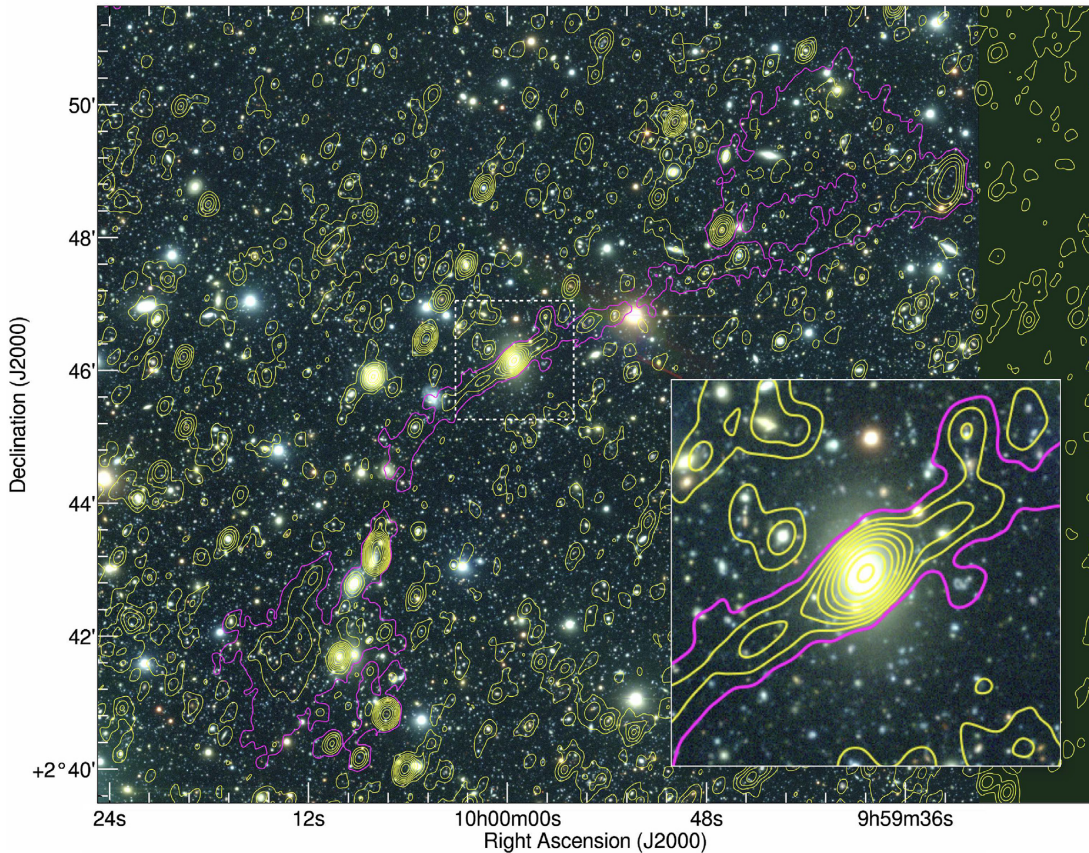


Figure 2. GRG1 as seen in MIGHTEE (yellow contours), overlaid on a composite optical image of HSC g , r , and i bands. Contours are shown at intervals of $30\sqrt{3}^n \mu\text{Jy beam}^{-1}$, where $n = 0, 1, 2, \dots, 20$. The lowest contour level is $7 \mu\text{Jy beam}^{-1}$ and is shown in magenta, as in Fig. 1, to highlight the full extent of the GRG. The inset shows an enlargement of the core area, where the host galaxy can be seen.

3.1.2 VLA-3GHz data

Only the core of GRG1 is clearly detected in the VLA-3GHz data and the total flux density reported for the object by Smolčić et al. (2017a) was 3.02 ± 0.15 mJy.

In these high-resolution VLA data, the core of the GRG is resolved and displays a double-lobed/jetted structure (see inset of Fig. 3). These could be the inner-most part of the jets, or could be a separate set of inner lobes/jets. In the latter case, this object could be classified as a double-double radio galaxy (e.g. Schoenmakers et al. 2000; Mahatma et al. 2019) and a candidate restarted AGN (e.g. Brienza et al. 2020; Jurlin et al. 2020 and references therein). However, no hotspots are evident in this region, as might be expected from inner lobes/jets.

The northern lobe/hotspot of GRG1 is detected in the 3 GHz data, as seen in Fig. 3. However, it has a low signal-to-noise ratio (SNR) and therefore does not appear in the $\text{SNR} \geq 5$ source catalogue presented by Smolčić et al. (2017a). There is only a vague hint of the southern lobe in the 3 GHz map, being highly diffuse and therefore predominantly resolved out of the VLA data.

3.1.3 Radio power

To determine the spectral index of the core, we first smooth the VLA-3GHz map to the resolution of the MIGHTEE map. We then measure the spectral index using the MIGHTEE peak brightness (3.73 ± 0.01 mJy beam $^{-1}$; to minimize contamination from the jets) and the 3 GHz peak brightness from the smoothed

map (2.93 ± 0.032 mJy beam $^{-1}$). This gives $\alpha_{3\text{GHz}}^{\text{eff}} = -0.51 \pm 0.03$. Here, $\nu_{\text{eff}} = 1.217$ GHz and is the effective frequency of the MIGHTEE map at the position of this GRG. The relative flatness of the core's spectrum is expected due to synchrotron self-absorption.

GRG1 has a 1.2 GHz radio power of $\sim 10^{24.4}$ W Hz $^{-1}$ (lower limit of $\sim 10^{24.1}$ W Hz $^{-1}$). This was calculated using the measured spectral index of the core and assuming a spectral index of -0.8 for the lobes. This assumption is reasonable for an optically thin lobe, and also given that Dabhade et al. (2020a) find the mean spectral index distribution of their sample of GRGs to be $\alpha_{0.144}^{1.4} = -0.79$, which is similar to that of RGs.

Although the morphology of GRG1 somewhat resembles an FRII-like structure, its radio power is more typical of an FRI-type galaxy (Fanaroff & Riley 1974). However, this is consistent with the results of Mingo et al. (2019) who have recently discovered a population of low-luminosity⁶ FRII-type RGs in LoTSS. They find that radio luminosity does not reliably predict whether a source has an FRI or an FRII-type morphology. Furthermore, GRG1 has a lower radio power than that of most known GRGs. According to Dabhade et al. (2020b), known GRGs at $z < 1.0$ have mean 1.4 GHz radio powers of $\sim 10^{25.3}$ W Hz $^{-1}$. In many ways, GRG1 is reminiscent of NGC 6251, a borderline FRI/FRII GRG. Both have weak hotspots, FRI-like jets, and radio powers below the FR break (Cantwell et al. 2020).

⁶Up to several orders of magnitude below the traditional FR break, which is $\sim 10^{24.5}$ W Hz $^{-1}$ in L band.

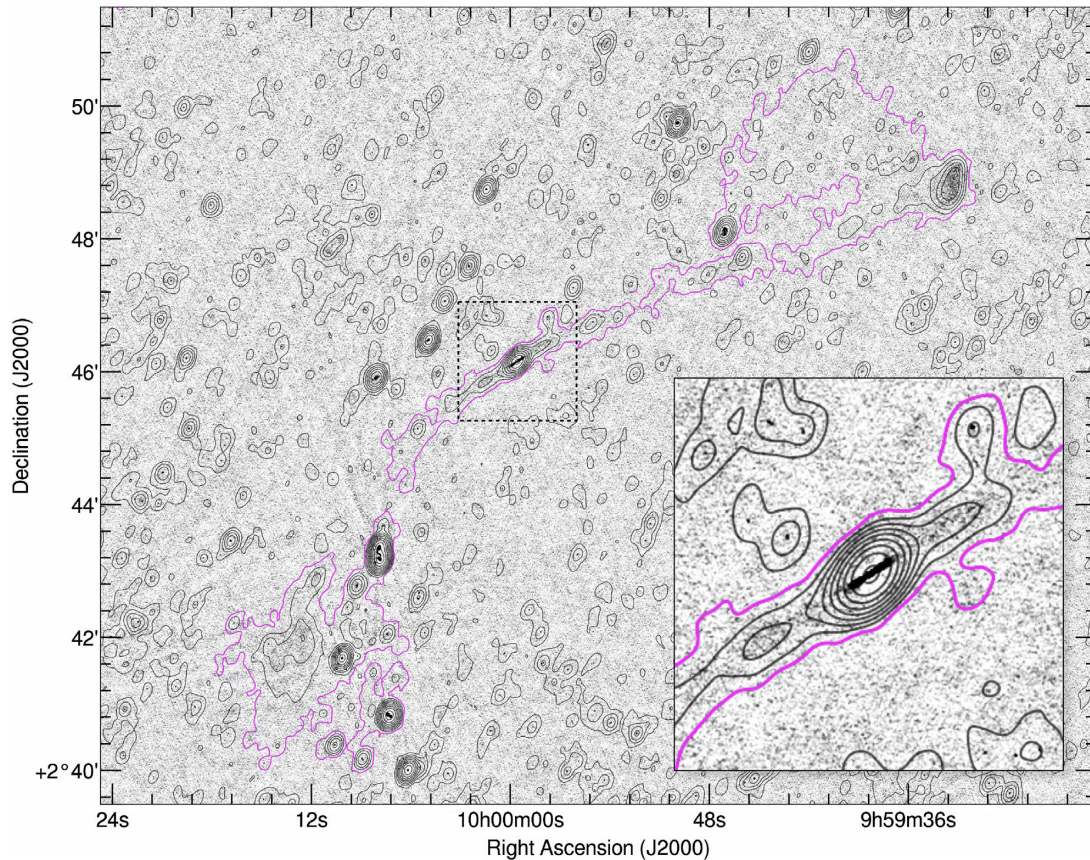


Figure 3. GRG1 as seen in the VLA-3 GHz data (background map) and in the MIGHTEE data (black contours). Contour levels are as in Fig. 2 and the lowest contour level is again shown in magenta. The hotspot in the northern lobe is seen faintly at 3 GHz. The inset shows an enlargement of the core region, where a double-lobed/jetted structure can be seen in the VLA-3GHz image.

3.1.4 Host galaxy and AGN characterization

The host galaxy of this radio source appears elliptical in Hyper Suprime-Cam imaging (Aihara et al. 2019; see Fig. 2 inset). The top panel of Fig. 4 shows the rest-frame SDSS DR14 optical spectrum of the host galaxy. Features typical of an early-type elliptical galaxy can be seen in this spectrum, such as a prominent 4000 Å break, the presence of strong absorption lines like Mg I and NaD, as well as the lack of nebular emission lines. It contains no prominent narrow or broad emission lines associated with high excitation radio galaxies or quasars, such as [O III].

To further examine whether there is any evidence of radiatively efficient AGN activity, we fit the spectral energy distribution (SED) of the host galaxy with various templates. The SED is constructed using the photometric catalogue of Laigle et al. (2016; hereafter COSMOS15), along with mid-infrared (including 24 μm) to sub-millimetre data from the ‘superdeblended’ catalogue of Jin et al. (2018). Note that the only significant detection (to the 3σ level) of GRG1 in *Herschel* bands⁷ is at 100 μm. The 3σ upper limits were used in cases of non-detection (see Delvecchio et al. 2017 for details).

The SED is fit with: (i) the MAGPHYS code of da Cunha, Charlot & Elbaz (2008) considering only star formation, and (ii) the SED3FIT code of Berta et al. (2013) which also incorporates a set of AGN

templates. The results are shown in Fig. 5 and further details of the SED-fitting approach can be found in Delvecchio et al. (2017). The fit obtained in the latter case, with an AGN component, does not significantly (<99 per cent confidence level) improve the reduced χ^2 of the fit, on the basis of a Fisher-test. Therefore, we conclude that SED fitting reveals no evidence of radiatively efficient AGN activity.

From the best-fitting parameters of the SED model (without AGN), we find that the host galaxy has a stellar mass of $M_* = 10^{11.42} M_\odot$ and a (combined IR and UV) star formation rate (SFR) of $1.97 M_\odot \text{ yr}^{-1}$. It is therefore only weakly star-forming and lies below the main sequence of star formation (Schreiber et al. 2015) by a factor of ~ 2 . This is consistent with the fact that it is undetected in the far-infrared.

In the X-ray regime, the galaxy has a [2–10] keV luminosity of $L_X \sim 10^{41.6} \text{ erg s}^{-1}$, based on data from the Chandra-COSMOS (Elvis et al. 2009; Civano et al. 2012) and COSMOS-Legacy catalogues (Civano et al. 2016; Marchesi et al. 2016). Since this is roughly five times in excess of that predicted by the SFR– $L_{X\text{-ray}}$ relation of star-forming galaxies (Lehmer et al. 2016), it is possible that concomitant low-luminosity AGN activity is present in the X-ray. The AGN bolometric luminosity predicted by the fit with AGN would be consistent within 1σ with the observed L_X , if assuming a set of [2–10] keV bolometric corrections from Lusso et al. (2012). However, the total X-ray emission from the core follows the correlation for unabsorbed jet-related emission in Hardcastle, Evans & Croston (2009). Therefore, this is likely a pure jet system with no evidence for additional accretion-related X-ray emission.

⁷Data from the Photoconductor Array Camera and Spectrometer Evolutionary Probe (PEP; Lutz et al. 2011) survey and *Herschel* Multitiered Extragalactic Survey (HerMES; Oliver et al. 2012).

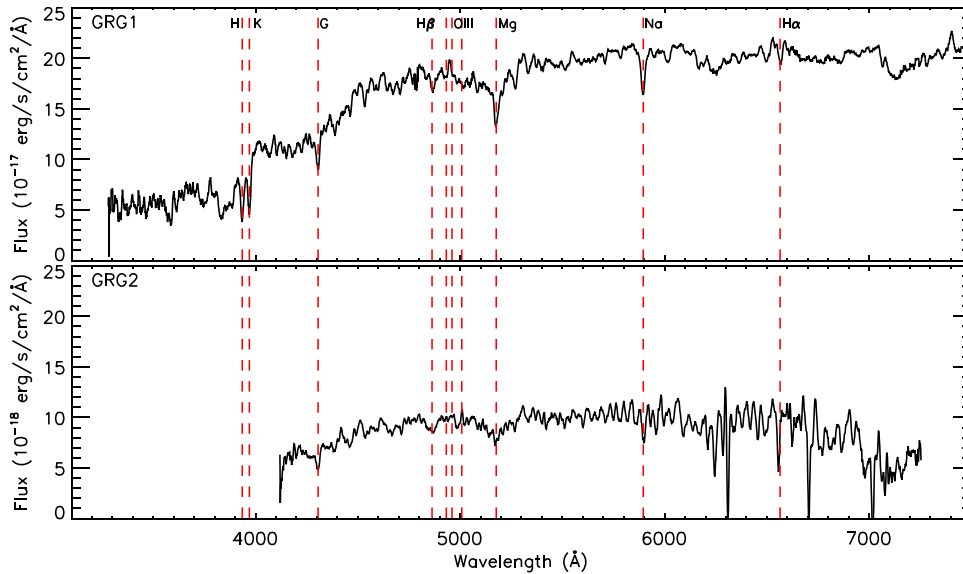


Figure 4. Rest-frame optical spectra of the GRG host galaxies. Top: SDSS DR14 spectrum for GRG1. Bottom: zCOSMOS spectrum for GRG2.

Therefore, no evidence of (obscured or unobscured) radiatively efficient AGN activity is found in any regime. Rather, GRG1 can be classified as a low-excitation radio AGN (LERG; e.g. Best & Heckman 2012) powered by radiatively inefficient Bondi accretion of hot gas from the IGM (Hardcastle & Croston 2020 and references therein) hosted by a massive, weakly star-forming elliptical galaxy.

The host of GRG1 is the most massive galaxy in a group of eight according to the zCOSMOS group catalogue of Knobel et al. (2012) (group ID 606). Furthermore, Giodini et al. (2010) associated the core of this galaxy with an X-ray cluster. This is unsurprising since GRGs are commonly found to reside in small groups of galaxies (Malarecki et al. 2015). This environmental information supports the scenario in which the bending of the southern jet, and the extended emission of the northern lobe, result from interactions with the surrounding intergalactic and intracluster medium of the GRG.

3.2 MGTC J100016.84+015133.0 (GRG2)

3.2.1 MIGHTEE data

GRG2 is shown in Figs 1, 6, and 7. The core is situated at RA = $10^{\text{h}}00^{\text{m}}16^{\text{s}}.84$ and Dec. = $+01^{\text{d}}51^{\text{m}}33^{\text{s}}.0$. The associated host galaxy has a spectroscopic redshift of $z = 0.3363$ according to the zCOSMOS Bright catalogue (Lilly et al. 2007, 2009).

Both lobes and a potential hotspot within the northern lobe are clearly detected for the first time in MIGHTEE, as is the entire northern jet and some weak emission from the southern jet. Based on these data, GRG2 has a projected angular size of 6.8 arcmin and therefore a projected linear size of 2.04 Mpc. Some elongated emission is seen in MIGHTEE between the core and the southern lobe, which may be attributable to the jet in that direction.

The unequal strength of detection of the two jets may imply that they are relativistic on these scales and lie away from the plane of the sky, so that their apparent surface brightness is being affected by relativistic beaming (Blandford & Königl 1979).

Flux densities have been measured within the region outlined by the magenta contour shown in Fig. 1.

3.2.2 VLA-3 GHz data

As seen in Fig. 7, there is a hint of a VLA-3 GHz detection of the northern lobe/hotspot, though it does not appear in the source catalogue of Smolčić et al. (2017a) due to its low SNR in these data. No hotspot is seen in the southern lobe in MIGHTEE and this lobe is entirely undetected in the VLA-3 GHz data.

The core is detected in the VLA-3 GHz observations and is reported in the source catalogue of Smolčić et al. (2017b) with a 3 GHz flux density of 0.878 ± 0.044 mJy. There is no evidence of any extended structure or unusual morphology of the core in these VLA data (see Fig. 7 inset).

3.2.3 Radio power

The MIGHTEE peak brightness of the GRG2 core (0.72 ± 0.01 mJy beam $^{-1}$) and the peak brightness from the smoothed VLA-3 GHz map (2.43 ± 0.03 mJy beam $^{-1}$) are used to find a spectral slope of $\alpha_{3\text{GHz}}^{1.256\text{GHz}} \sim 0.29 \pm 0.04$. This is relatively flat, although slightly positive and is again consistent with typical cores of radio galaxies. Considering this and again assuming a spectral index of -0.8 for the lobes, the 1.2 GHz radio power of GRG2 is $\sim 10^{24.1}$ W Hz $^{-1}$. This is lower than most known GRGs (Dabhade et al. 2020b) and slightly lower than that of GRG1.

3.2.4 Host galaxy and AGN characterization

The host galaxy appears elliptical in HSC imaging (see Fig. 6 inset). Despite having a zCOSMOS optical spectrum of relatively poor quality (bottom panel of Fig. 4), it is typical of the absorption spectrum of a red, dead elliptical galaxy, with no emission features present.

GRG2 displays no signatures of AGN activity in the X-ray or mid-IR and has no significant detection in the superdeblended *Herschel* photometry of Jin et al. (2018), with a combined SNR of all *Herschel* bands of only ~ 0.8 . It is not identified as an AGN via SED fitting (see Fig. 5). Note that the SED fit is not improved by the inclusion of an AGN template despite the improvement at $24 \mu\text{m}$, since the outcome of the Fisher-test is guided much more by the worsening of the fit at IRAC- $8 \mu\text{m}$. If the fit with AGN was preferred, the predicted

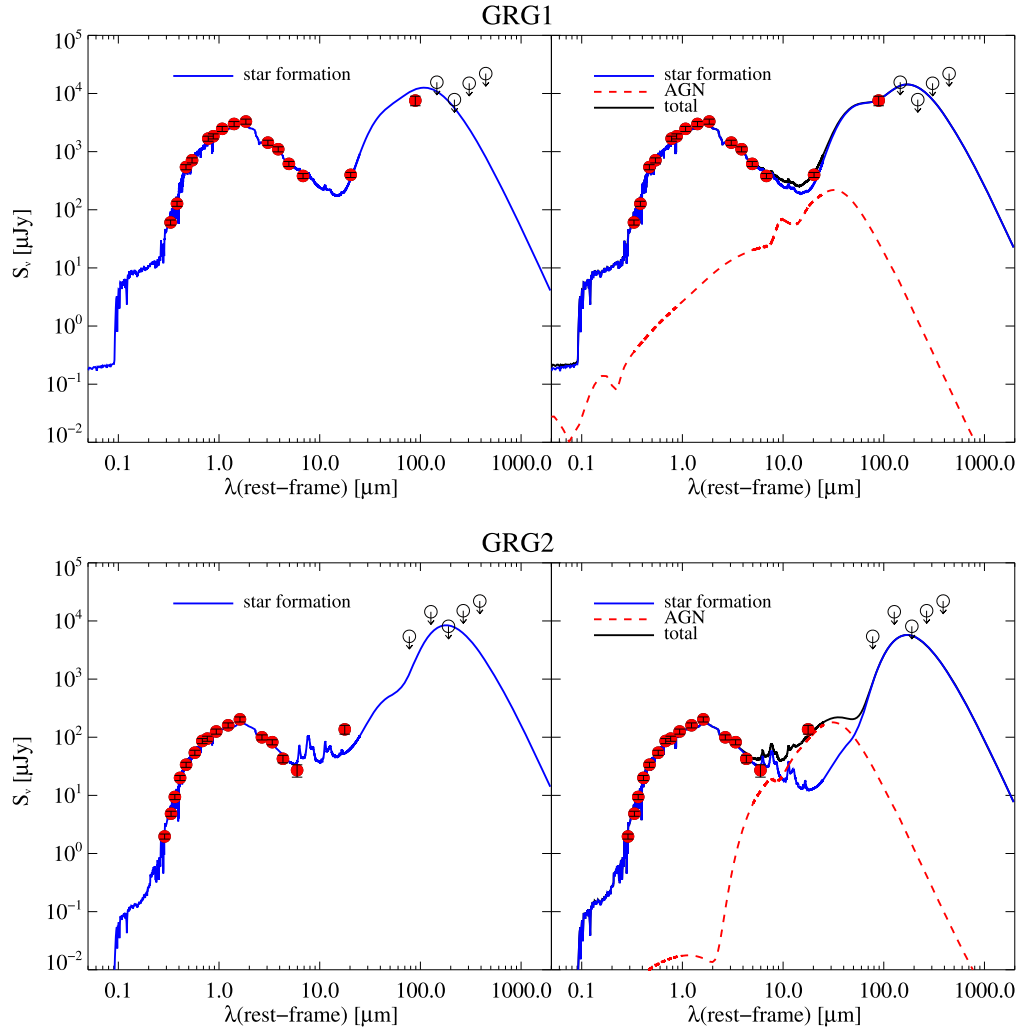


Figure 5. SED of the GRG1 (top) and GRG2 (bottom) host galaxies showing detections (closed points) or 3σ upper limits (open circles) in UV to sub-millimetre bands. The best-fitting template considering only star formation (blue line) was determined using MAGPHYS (left) and SED3FIT (right). SED3FIT also fits an AGN template (dashed red line), and the combined (AGN + star-forming) template (black line). The MAGPHYS fit on the left was preferred for both GRGs, based on a Fisher-test of the reduced χ^2 . See text for further details.

AGN bolometric luminosity would correspond to an expected $L_X \sim 10^{42.6}$ erg s $^{-1}$, which is about 10 times higher than the formal X-ray limit at [2–10] keV (Civano et al. 2016). Since GRG2 is not X-ray detected, this check further supports the relatively low significance of the AGN component obtained from the Fisher-test.

The host galaxy of GRG2 has a stellar mass of $M_* = 10^{10.8} M_\odot$ and an SFR of $\sim 0.5 M_\odot \text{ yr}^{-1}$, placing it well below the main sequence of star formation. Its quiescent nature is further supported by its classification as ‘red’ based on its ($NUV - r$) and ($r - J$) colours in COSMOS2015.

We therefore conclude that GRG2, like GRG1, is a radiatively inefficient LERG with a massive, red, passive elliptical host. This is in line with expectations since LERGs tend to be hosted by galaxies which have redder colours, larger stellar masses and lower SFRs than HERG hosts (e.g. Best & Heckman 2012; Hardcastle et al. 2013). Little information currently exists about the SFRs of GRGs specifically, however Clarke et al. (2017) and Dabhade et al. (2020c) have found evidence for moderate SFRs in several individual GRG hosts.

GRG2 resides in a smaller, less rich group than GRG1. The GRG2 host is the most massive of the five galaxies in the group (group ID 753; Knobel et al. 2012).

We note that the compact source to the south-west of centre (labelled in Fig. 1) was also investigated as a potential position of the GRG core. However, it is not situated close to the equidistant centre of the lobes and the associated optical counterpart has a photometric redshift of $z = 2.015$ in COSMOS15, so is less likely to be the GRG host. It is considered an unrelated compact source and its contribution to the total flux density of the southern lobe has been removed.

4 DISCUSSION

4.1 Statistics and GRG sky density

Dabhade et al. (2020b) find that GRGs with sizes > 2 Mpc are extremely rare and comprise only 9 percent of the GRG population at $z < 1$. We now estimate the probability of finding two > 2 Mpc GRGs in such a small (1 deg 2) sky area. For this purpose, our selection criteria can be considered to be GRGs with projected linear sizes > 2 Mpc out to a redshift of $z = 0.5$ (and therefore with angular sizes of > 5.3 arcmin).

We compare with the GRG sample of Dabhade et al. (2020a). They provide the most extensive survey of GRGs to-date, and therefore the

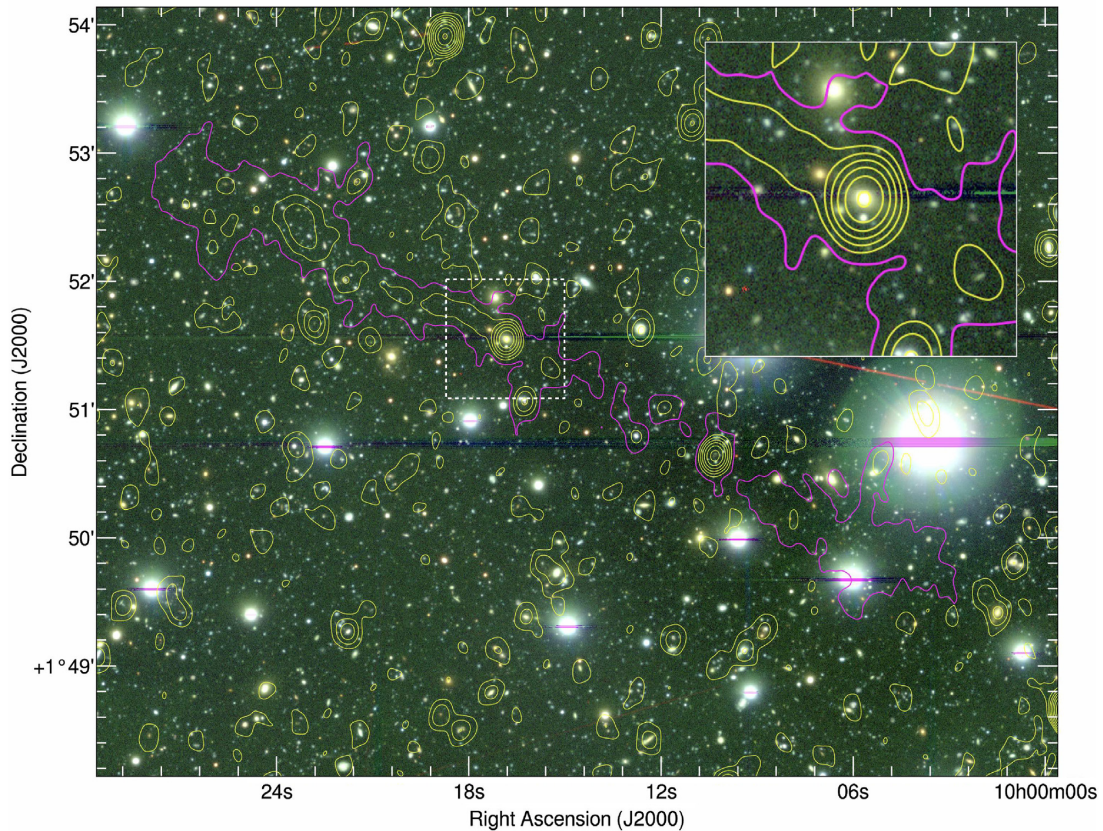


Figure 6. GRG2 as seen in MIGHTEE (yellow contours), overlaid on a composite optical image of HSC g , r , and i bands. Contours are shown at intervals of $20\sqrt{3}^n \mu\text{Jy beam}^{-1}$, where $n = 0, 1, 2, \dots, 20$. The lowest contour level is $5 \mu\text{Jy beam}^{-1}$ and is shown in magenta, as in Fig. 1, to highlight the full extent of the GRG. The inset shows an enlargement of the core area.

most robust sky density estimate presently available. Dabhade et al. (2020a) found 239 GRGs over a 424 deg^2 sky area using the LoTSS survey. Only seven of these have sizes larger than 2 Mpc, of which only one has $z < 0.5$. This gives a sky density of 0.0023 GRGs per deg^2 for such objects.

We first assume that this sky density is the ‘true’ GRG sky density of the Universe. We also assume independence of repeated events. That is, that the presence of one GRG in the sky area does not affect whether or not another is present, which is likely given the very different redshifts of the two GRGs presented here. We can thus employ Poisson statistics to estimate the probability (P) of finding k number of GRGs in a 1 deg^2 sky area:

$$P(X = k) = \frac{\lambda^k e^{-\lambda}}{k!}, \quad (1)$$

where λ is the expected number of occurrences and is equal to 0.0023 (which is the GRG sky density expected from the results of Dabhade et al. 2020a, as above). For the case of $k = 2$, we find $P(X \geq 2) = 2.7 \times 10^{-6}$. Therefore, there is a probability of 2.7×10^{-6} of finding two or more GRGs with projected linear sizes $> 2 \text{ Mpc}$ at $z < 0.5$ within a 1 deg^2 field, given our initial assumptions.

If the observed sky region is not strongly affected by cosmic (sample) variance or other significant selection effects, the small p -value we find implies that either we have been exceptionally lucky in finding these two objects, or that our initial assumption does not hold and the true GRG sky density is significantly higher than previously known.

The most likely explanation for an underestimated GRG sky density is the limited sensitivity to extended, diffuse emission of GRG lobes in past surveys. For example, LoTSS is incomplete to low-luminosity giants due to surface brightness sensitivity limitations, as illustrated in fig. 8 of Hardcastle et al. (2019). While the components of GRG1 and GRG2 would exceed the 5σ sensitivity limit of LoTSS, it would be difficult to identify these components as belonging to the same system if the low surface brightness emission joining them is not visible.

While the uv coverage and angular resolution of LOFAR and MeerKAT are comparable, the point source sensitivity of MIGHTEE ($\sim 11 \mu\text{Jy}$ at 144 MHz, for $\alpha = -0.8$) is significantly deeper than LoTSS ($\sim 71 \mu\text{Jy}$ at 144 MHz). While it is non-trivial to directly compare surface brightness sensitivities of the two surveys, MIGHTEE is expected to be superior due to its depth. Low-frequency surveys do benefit from being more sensitive to the steepest spectrum lobe emission of GRGs, however LoTSS would only surpass MIGHTEE in sensitivity where the spectral index is steeper than $\alpha \approx -1.7$.

A further explanation for a previously underestimated GRG sky density is a dearth of highly sensitive, ancillary multiwavelength observations. This would make it more difficult to determine whether or not lobes and hotspots are associated with separate near-infrared/optical counterparts, particularly at higher redshifts. This issue is largely avoided by MIGHTEE-COSMOS thanks to the wealth of high-quality multiwavelength data available in the field.

Therefore, GRGs may be yet more numerous than presently known, despite the rapid increase in the number of these giants

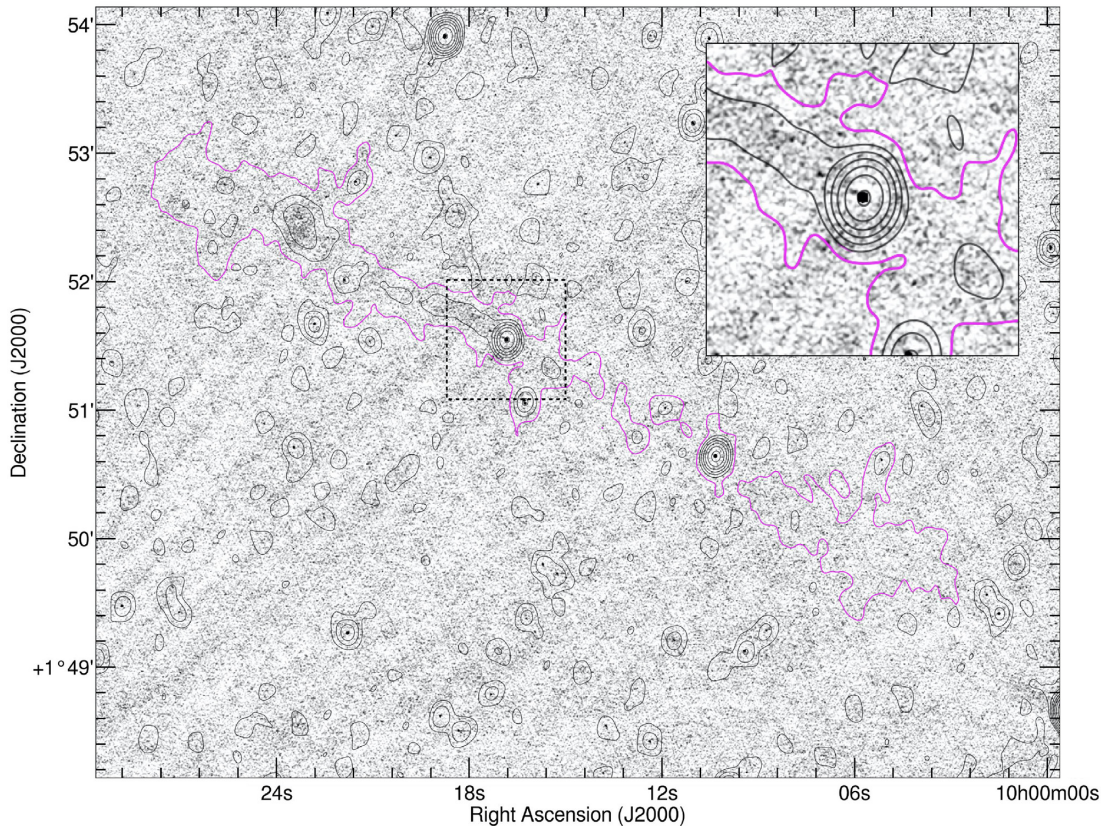


Figure 7. GRG2 as seen in the VLA-3 GHz data (background map) and in the MIGHTEE data (black contours). Contour levels as in Fig. 2. At 3 GHz, a compact core is seen and diffuse emission in the northern hotspot is faintly visible.

discovered in recent years (e.g. Dabhade et al. 2020a, b). This has also been suggested by other works, such as Ishwara-Chandra et al. (2020) who discovered six new ~ 1 Mpc-sized GRGs out to $z \sim 1.3$ in the ELAIS North 1 field with the GMRT.

4.2 GRG parameter space

GRG1 and GRG2 do not seem atypical of large radio galaxies in that they are LERGs hosted by ‘red and dead’ elliptical galaxies, have flat spectrum cores and exist in unremarkable environments (see Hardcastle & Croston 2020 for a review of radio AGN properties).

They do, however, have larger sizes and lower radio powers than most known GRGs. In fact, they lie in a heretofore unoccupied part of the GRG power-size (P – D) diagram. This is shown in Fig. 8, in comparison to the 780 GRGs from the compilation catalogue of Dabhade et al. (2020b) for which L -band flux measurements are available from the NVSS or the literature (Dabhade, private communication). For these, 1.2 GHz radio powers have been calculated using the measured spectral index where available, or otherwise assuming a value of $\alpha = -0.8$.

Note that the lower limit (and likely more realistic) radio power of GRG1 ($P_{1.2} = 10^{24.1}$ W Hz $^{-1}$; see Section 3.1.3) has been used in Fig. 8. However, GRG1 would still sit slightly below all other GRG of the same size on this diagram if the conservative upper limit to its radio power was used.

It is therefore possible that these new MIGHTEE observations are uncovering an unexplored realm of GRG parameter space, hitherto invisible to previous surveys due to the limitations discussed in Section 4.1. These may be the low-luminosity giants predicted by

the P – D tracks of, for example, Kaiser et al. (1997), Shabala et al. (2008), and Hardcastle et al. (2019).

To illustrate this, Fig. 8 also shows the evolutionary tracks of radio galaxies of various jet powers, as determined by Hardcastle et al. (2019). These are shown for an environment of halo mass $10^{13} M_{\odot}$, observing frequency 1.2 GHz and $z = 0.25$. GRG1 and GRG2 are consistent with the evolution of a $\sim 10^{37.5}$ W jet after ~ 700 Myr, under these conditions.

4.3 Implications

While our analysis has considered only enormous (> 2 Mpc) objects, if radio galaxies must grow to reach this size, then we may expect to similarly uncover in our data previously undetected GRGs with smaller sizes. The full 20 deg^2 MIGHTEE survey will provide an excellent resource for such studies when it is completed in the near future. Based on the GRG sky density, we observe in COSMOS (2 per deg^2), we could uncover ~ 40 GRGs with the full survey. With MeerKAT simultaneously facilitating excellent sensitivity, sky coverage and uv coverage with relatively high resolution, and the upcoming Square Kilometre Array (SKA) providing even better angular resolution, we may expect to discover many more diffuse, extended GRGs in the near- to mid-future.

The existence of a larger population of GRGs may have implications for our understanding of the AGN duty cycle. Low-frequency follow-up observations of these objects can provide spatially resolved spectral information, which will help us to characterize the intermittency of the radio AGN activity. Such information is crucial for our understanding of whether AGN feedback across subsequent

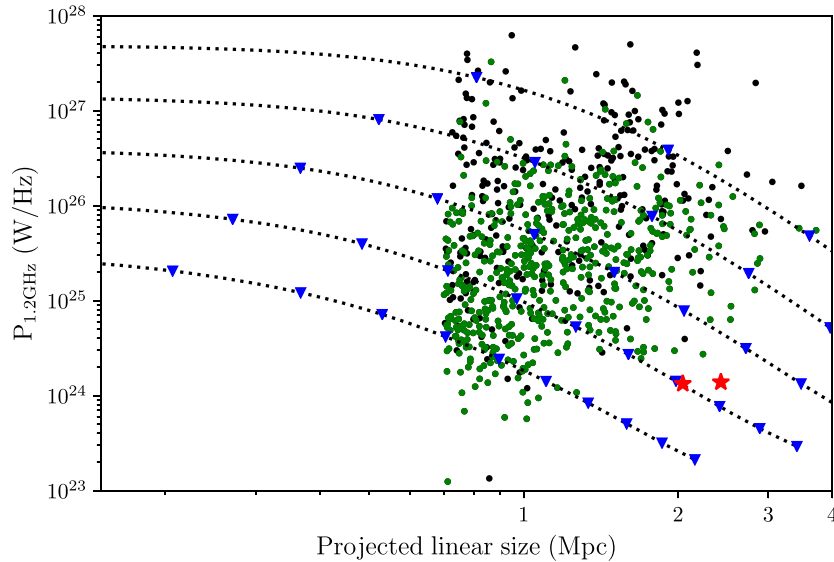


Figure 8. The position in the 1.2 GHz power-size (P - D) diagram of almost all known GRGs. Objects in the compilation catalogue of Dabhade et al. (2020b) are shown as green ($z < 0.5$) and black ($z \geq 0.5$) points. GRG1 and GRG2 are shown as red stars and are located in a previously unoccupied part of this diagram. For comparison, dotted lines show evolutionary tracks as determined by Hardcastle et al. (2019) for radio galaxies with jet powers of (bottom to top) 10^{37} , $10^{37.5}$, 10^{38} , $10^{38.5}$, and 10^{39} W. The tracks show a lifetime of up to 1 Gyr with blue triangles marking each hundred Myr. GRG1 and GRG2 are consistent with the evolution of a $\sim 10^{37.5}$ W jet after ~ 700 Myr.

accretion episodes remains constant or decreases with time, enabling predictions of the overall life cycle of AGN activity relative to the host. This is essential for advancing our current understanding of the extent to which AGN-driven mechanical feedback can alter the star-forming content of the host galaxy (Croton et al. 2006).

5 CONCLUSIONS

Thanks to the impressive capabilities of the MeerKAT telescope, two new giant radio galaxies have been identified in a 1 deg^2 MIGHTEE survey of the COSMOS field. Both are ‘red and dead’ LERGs and are among the largest known GRGs with sizes of > 2 Mpc. However, they have low radio powers that place them in a previously unpopulated part of GRG parameter space. Due to the diffuse nature of the jets and lobes, these objects were resolved out and undetected in previous surveys of the COSMOS field, including sensitive 3 GHz observations with the VLA.

The probability of finding at least two such GRGs in a small, 1 deg^2 field is only 2.7×10^{-6} , based on wide-field observations with LOFAR. Therefore, our findings provide strong evidence that GRGs may be far more numerous than previously thought. It is only with new radio surveys such as MIGHTEE, providing excellent extended brightness sensitivity, that this ‘hidden’ population of GRGs can be revealed. Systematic searches across the full MIGHTEE survey are expected to yield detections of many more GRGs and low-frequency follow-up can help reveal important information about the AGN duty cycle. These are tantalizing hints of what the future SKA will ultimately uncover with its simultaneously excellent angular resolution and surface brightness sensitivity.

ACKNOWLEDGEMENTS

We thank the anonymous referee for providing useful comments that have strengthened the paper. We thank Pratik Dabhade for helpful discussions and for generously providing their GRG catalogue. The

MeerKAT telescope is operated by the South African Radio Astronomy Observatory (SARAO; www.ska.ac.za), which is a facility of the National Research Foundation (NRF), an agency of the Department of Science and Innovation. JD, SVW, IH, and MP acknowledge the financial assistance of SARAO. MP, SMR, and LL acknowledge the financial assistance of the NRF. Opinions expressed and conclusions arrived at, are those of the authors and are not necessarily to be attributed to the NRF.

MJJ and IH acknowledge support from the UK Science and Technology Facilities Council [ST/N000919/1]. MJJ, IH, and IHW acknowledge support from the Oxford Hintze Centre for Astrophysical Surveys that is funded through generous support from the Hintze Family Charitable Foundation. IH thanks the Rhodes University Centre for Radio Astronomy Techniques and Technologies (RATT) for the provision of computing facilities. ID is supported by the European Union’s Horizon 2020 research and innovation program under the Marie Skłodowska-Curie grant agreement no. 788679. MP, JC, FXA, MV, KT, and MG acknowledge financial support from the Inter-University Institute for Data Intensive Astronomy (IDIA). The research of OS is supported by the South African Research Chairs Initiative of the NRF. YA acknowledges support by NSFC grant 11933011. RB acknowledges support from the Glasstone Foundation. MB, LM, MV, and IP acknowledge financial support from the Italian Ministry of Foreign Affairs and International Cooperation (MAECI Grant Number ZA18GR02) and the South African NRF (Grant Number 113121) as part of the ISARP RADIOSKY2020 Joint Research Scheme. JA acknowledges financial support from the Science and Technology Foundation (FCT, Portugal) through research grants PTDC/FIS-AST/29245/2017, UID/FIS/04434/2019, UIDB/04434/2020, and UIDP/04434/2020. NA acknowledges funding from the Science and Technology Facilities Council (STFC) Grant Code ST/R505006/1. ZR acknowledges financial support from the South African Astronomical Observatory that is a facility of the South African NRF. NM acknowledges support from the Bundesministerium für Bildung und Forschung (BMBF) D-MeerKAT

award 05A2017. KT acknowledges support from the Inter-University Institute for Data Intensive Astronomy (IDIA). MB acknowledges support from the ERC-Stg DRANOEL, no. 714245.

We acknowledge the use of the Ilifu cloud computing facility – www.ilifu.ac.za, a partnership between the University of Cape Town, the University of the Western Cape, the University of Stellenbosch, Sol Plaatje University, the Cape Peninsula University of Technology, and the South African Radio Astronomy Observatory. The Ilifu facility is supported by contributions from the Inter-University Institute for Data Intensive Astronomy (IDIA – a partnership between the University of Cape Town, the University of Pretoria and the University of the Western Cape), the Computational Biology division at UCT, and the Data Intensive Research Initiative of South Africa (DIRISA). This work made use of the CARTA (Cube Analysis and Rendering Tool for Astronomy) software (DOI 10.5281/zenodo.3377984 – <https://cartavis.github.io>).

The Hyper Suprime-Cam (HSC) collaboration includes the astronomical communities of Japan and Taiwan, and Princeton University. The HSC instrumentation and software were developed by the National Astronomical Observatory of Japan (NAOJ), the Kavli Institute for the Physics and Mathematics of the Universe (Kavli IPMU), the University of Tokyo, the High Energy Accelerator Research Organization (KEK), the Academia Sinica Institute for Astronomy and Astrophysics in Taiwan (ASIAA), and Princeton University. Funding was contributed by the FIRST program from Japanese Cabinet Office, the Ministry of Education, Culture, Sports, Science and Technology (MEXT), the Japan Society for the Promotion of Science (JSPS), Japan Science and Technology Agency (JST), the Toray Science Foundation, NAOJ, Kavli IPMU, KEK, ASIAA, and Princeton University.

DATA AVAILABILITY

The data underlying this article were accessed from the South African Radio Astronomy Observatory (SARAO; www.ska.ac.za). The derived data generated in this research will be shared on reasonable request to the corresponding author.

REFERENCES

- Abolfathi B. et al., 2018, *ApJS*, 235, 42
 Aihara H. et al., 2019, *PASJ*, 71, 114
 Asad K. M. B. et al., 2019, preprint ([arXiv:1904.07155](https://arxiv.org/abs/1904.07155))
 Becker R. H., White R. L., Helfand D. J., 1995, *ApJ*, 450, 559
 Berta S. et al., 2013, *A&A*, 551, A100
 Best P. N., Heckman T. M., 2012, *MNRAS*, 421, 1569
 Blandford R. D., Königl A., 1979, *ApJ*, 232, 34
 Brienza M. et al., 2020, *A&A*, 638, A29
 Cantwell T. M. et al., 2020, *MNRAS*, 495, 153
 Chabrier G., 2003, *PASP*, 115, 763
 Civano F. et al., 2012, *ApJS*, 201, 30
 Civano F. et al., 2016, *ApJ*, 819, 62
 Clarke A. O. et al., 2017, *A&A*, 601, A25
 Condon J. J., Cotton W. D., Greisen E. W., Yin Q. F., Perley R. A., Taylor G. B., Broderick J. J., 1998, *AJ*, 115, 1693
 Cotton W. D. et al., 2020, *MNRAS*, 495, 1271
 Croton D. J. et al., 2006, *MNRAS*, 365, 11
 Dabhade P., Gaikwad M., Bagchi J., Pandey-Pommier M., Sankhyayan S., Raychaudhury S., 2017, *MNRAS*, 469, 2886
 Dabhade P. et al., 2020a, *A&A*, 635, A5
 Dabhade P. et al., 2020b, *A&A*, 642, A153
 Dabhade P., Combes F., Salomé P., Bagchi J., Mahato M., 2020c, *A&A*, 643, A111
 da Cunha E., Charlot S., Elbaz D., 2008, *MNRAS*, 388, 1595
 Delvecchio I. et al., 2017, *A&A*, 602, A3
 Elvis M. et al., 2009, *ApJS*, 184, 158
 Fanaroff B. L., Riley J. M., 1974, *MNRAS*, 167, 31P
 Giodini S. et al., 2010, *ApJ*, 714, 218
 Gupta Y. et al., 2017, *Curr. Sci.*, 113, 707
 Hardcastle M. J., Croston J. H., 2020, *New Astron. Rev.*, 88, 101539
 Hardcastle M. J., Evans D. A., Croston J. H., 2009, *MNRAS*, 396, 1929
 Hardcastle M. J. et al., 2013, *MNRAS*, 429, 2407
 Hardcastle M. J. et al., 2016, *MNRAS*, 462, 1910
 Hardcastle M. J. et al., 2019, *A&A*, 622, A12
 Heywood I., 2020, Astrophysics Source Code Library, record ascl:2009.003
 Hurley-Walker N. et al., 2015, *MNRAS*, 447, 2468
 Ishwara-Chandra C. H., Saikia D. J., 1999, *MNRAS*, 309, 100
 Ishwara-Chandra C. H., Taylor A. R., Green D. A., Stil J. M., Vaccari M., Ocran E. F., 2020, *MNRAS*, 497, 5383–5394
 Jarvis M. et al., 2016, in *MeerKAT Science: On the Pathway to the SKA. Proceedings of Science, Stellenbosch*, p. 6
 Jin S. et al., 2018, *ApJ*, 864, 56
 Jonas J., MeerKAT Team, 2016, in *MeerKAT Science: On the Pathway to the SKA. Proceedings of Science, Stellenbosch*, p. 1
 Jurlin N. et al., 2020, *A&A*, 638, A34
 Kaiser C. R., Dennett-Thorpe J., Alexander P., 1997, *MNRAS*, 292, 723
 Knobel C. et al., 2012, *ApJ*, 753, 121
 Komberg B. V., Pashchenko I. N., 2009, *Astron. Rep.*, 53, 1086
 Laigle C. et al., 2016, *ApJS*, 224, 24
 Lan T.-W., Prochaska J. X., 2020, preprint ([arXiv:2009.04482](https://arxiv.org/abs/2009.04482))
 Lara L., Cotton W. D., Feretti L., Giovannini G., Marcaide J. M., Márquez I., Venturi T., 2001, *A&A*, 370, 409
 Lehmer B. D. et al., 2016, *ApJ*, 825, 7
 Lilly S. J., Le Fevre O., Renzini A., Zamorani G., Scodreggio M., Contini T., 2007, *ApJS*, 172, 70
 Lilly S. J. et al., 2009, *ApJS*, 184, 218
 Lusso E. et al., 2012, *MNRAS*, 425, 623
 Lutz D. et al., 2011, *A&A*, 532, A90
 Machalski J., Koziel-Wierzbowska D., Jamroz M., Saikia D. J., 2008, *ApJ*, 679, 149
 Mack K. H., Klein U., O’Dea C. P., Willis A. G., Saripalli L., 1998, *A&A*, 329, 431
 Mahatma V. H. et al., 2019, *A&A*, 622, A13
 Malarecki J. M., Jones D. H., Saripalli L., Staveley-Smith L., Subrahmanyan R., 2015, *MNRAS*, 449, 955
 Marchesi S. et al., 2016, *ApJ*, 830, 100
 Mauch T., Murphy T., Buttery H. J., Curran J., Hunstead R. W., Piestrzynski B., Robertson J. G., Sadler E. M., 2003, *MNRAS*, 342, 1117
 McMullin J. P., Waters B., Schiebel D., Young W., Golap K., 2007, in Shaw R. A., Hill F., Bell D. J., eds, *ASP Conf. Ser. Vol. 376, Astronomical Data Analysis Software and Systems XVI. Astron. Soc. Pac.*, San Francisco, p. 127
 Mingo B. et al., 2019, *MNRAS*, 488, 2701
 Offringa A. R. et al., 2014, *MNRAS*, 444, 606
 Oliver S. J. et al., 2012, *MNRAS*, 424, 1614
 Perley R. A., Chandler C. J., Butler B. J., Wrobel J. M., 2011, *ApJ*, 739, L1
 Planck Collaboration XIII et al., 2016, *A&A*, 594, A13
 Prescott M. et al., 2018, *MNRAS*, 480, 707
 Proctor D. D., 2016, *ApJS*, 224, 18
 Rengelink R. B., Tang Y., de Bruyn A. G., Miley G. K., Bremer M. N., Röttgering H. J. A., Bremer M. A. R., 1997, *A&AS*, 124, 259
 Schoenmakers A. P., de Bruyn A. G., Röttgering H. J. A., van der Laan H., Kaiser C. R., 2000, *MNRAS*, 315, 371
 Schoenmakers A. P., de Bruyn A. G., Röttgering H. J. A., van der Laan H., 2001, *A&A*, 374, 861
 Schreiber C. et al., 2015, *A&A*, 575, A74
 Seymour N. et al., 2020, *PASA*, 37, e013
 Shabala S. S., Ash S., Alexander P., Riley J. M., 2008, *MNRAS*, 388, 625
 Shimwell T. W. et al., 2019, *A&A*, 622, A1
 Smirnov O. M., Tasse C., 2015, *MNRAS*, 449, 2668
 Smolčić V. et al., 2017a, *A&A*, 602, A1
 Smolčić V. et al., 2017b, *A&A*, 602, A2

- Subrahmanyan R., Saripalli L., Safouris V., Hunstead R. W., 2008, *ApJ*, 677, 63
- Tang H., Scaife A. M. M., Wong O. I., Kapińska A. D., Rudnick L., Shabala S. S., Seymour N., Norris R. P., 2020, *MNRAS*, 499, 68
- Tasse C. et al., 2018, *A&A*, 611, A87
- Tingay S. J. et al., 2013, *PASA*, 30, e007
- van Haarlem M. P. et al., 2013, *A&A*, 556, A2
- Willis A. G., Strom R. G., Wilson A. S., 1974, *Nature*, 250, 625
- ¹Department of Astronomy, University of Cape Town, Private Bag X3, Rondebosch 7701, South Africa
- ²Astrophysics, Department of Physics, University of Oxford, Keble Road, Oxford OX1 3RH, UK
- ³Department of Physics and Electronics, Rhodes University, PO Box 94, Makhanda 6140, South Africa
- ⁴South African Radio Astronomy Observatory, 2 Fir Street, Black River Park, Observatory, Cape Town 7925, South Africa
- ⁵Inter-University Institute for Data Intensive Astronomy, and Department of Physics and Astronomy, University of the Western Cape, Robert Sobukwe Road, 7535 Bellville, Cape Town, South Africa
- ⁶Department of Physics and Astronomy, University of the Western Cape, Robert Sobukwe Road, 7535 Bellville, Cape Town, South Africa
- ⁷CEA, IRFU, DAp, AIM, Université Paris-Saclay, Université de Paris, CNRS, F-91191 Gif-sur-Yvette, France
- ⁸INAF – Osservatorio Astronomico di Brera, via Brera 28, I-20121 Milano, Italy
- ⁹Centre for Astrophysics Research, Department of Physics, Astronomy and Mathematics, University of Hertfordshire, College Lane, Hatfield AL10 9AB, UK
- ¹⁰CSIRO Astronomy and Space Science, PO Box 1130, Bentley, WA 6102, Australia
- ¹¹Instituto de Astrofísica e Ciências do Espaço, Universidade de Lisboa, OAL, Tapada da Ajuda, P-1349-018 Lisboa, Portugal
- ¹²Departamento de Física, Faculdade de Ciências, Universidade de Lisboa, Edifício C8, Campo Grande PT1749-016 Lisbon, Portugal
- ¹³Purple Mountain Observatory and Key Laboratory for Radio Astronomy, Chinese Academy of Sciences, 8 Yuanhua Road, 210034, Nanjing, China
- ¹⁴School of Astronomy and Space Science, University of Science and Technology of China, Hefei, Anhui, 230026, China
- ¹⁵Dipartimento di Fisica e Astronomia, Università di Bologna, via P. Gobetti 93/2, I-40129 Bologna, Italy
- ¹⁶INAF, Istituto di Radioastronomia, Via Gobetti 101, I-40129 Bologna, Italy
- ¹⁷Hamburger Sternwarte, University of Hamburg, Gojenbergsweg 112, D-21029 Hamburg, Germany
- ¹⁸The Inter-University Institute for Data Intensive Astronomy (IDIA), Department of Astronomy, University of Cape Town, Private Bag X3, Rondebosch 7701, South Africa
- ¹⁹School of Science, Western Sydney University, Locked Bag 1797, Penrith, NSW 2751, Australia
- ²⁰Faculty of Physics, Ludwig-Maximilians-Universität, Scheinerstr 1, D-81679 Munich, Germany
- ²¹Centre for Extragalactic Astronomy, Department of Physics, Durham University, Durham DH1 3LE, UK
- ²²South African Astronomical Observatory, PO Box 9, Observatory 7935, Cape Town, South Africa
- ²³National Radio Astronomy Observatory, 1003 Lopezville Road, Socorro, NM 87801, USA
- ²⁴A&A, Department of Physics, Faculty of Sciences, University of Antananarivo, B.P. 906, Antananarivo 101, Madagascar
- ²⁵Department of Physics, University of Pretoria, Private Bag X20, Hatfield 0028, South Africa
- ²⁶International Centre for Radio Astronomy Research, Curtin University, Bentley, WA 6102, Australia
- ²⁷GEPI, Observatoire de Paris, CNRS, Université Paris Diderot, 5 place Jules Janssen, F-92190 Meudon, France
- ²⁸Centre for Radio Astronomy Techniques and Technologies, Department of Physics and Electronics, Rhodes University, Grahamstown 6140, South Africa
- ²⁹USN, Observatoire de Paris, CNRS, PSL, UO, Nançay, 18330, France

This paper has been typeset from a $\text{\TeX}/\text{\LaTeX}$ file prepared by the author.